Supplement of Ocean Sci., 21, 2305–2344, 2025
https://doi.org/10.5194/os-21-2305-2025-supplement


Ocean Science Open Access EGU

*Supplement of*

# Mesoscale dynamics of an intrathermocline eddy in the Canary Eddy Corridor

**Luis P. Valencia et al.**

*Correspondence to:* Luis P. Valencia (luis.valencia102@alu.ulpgc.es)

# Supplements Overview

The following supplementary sections provide additional technical detail, sensitivity analyses, and methodological justifications that complement the main manuscript. Each section addresses a specific aspect of the dataset quality, spatial integration, or interpretation of the Bentayga eddy dynamics.

- **S1**: Sampling synopticity and Doppler-induced distortion.
- **S2**: Idealized eddy reconstruction from quasi-synoptic sections.
- **S3**: Radial zonation based on hydrographic and velocity structure.
- **S4**: Sensitivity of integrated budgets to domain boundaries.
- **S5**: Justification for core-limited integration using OceT.
- **S6**: Concluding remarks on methodological robustness.
- **S7**: Supplementary Video – Life cycle of the Bentayga eddy

All altimetric eddy metrics used in this supplementary study—including eddy trajectory, center position, and the perimeter corresponding to the maximum circum-averaged geostrophic speed—were obtained from the near-real-time (NRT) product META3.2exp distributed by AVISO+ (SSALTO/DUACS) (https://www.aviso.altimetry.fr). Further details are provided in the main manuscript.

# S1: Sampling synopticity and Doppler-induced distortion

During the eIMPACT2 survey, an intrathermocline eddy named *Bentayga* was extensively sampled aboard the R/V *Sarmiento de Gamboa*. The sampling strategy comprised several phases, two of which are included in the present study.

One of the main concerns raised by an anonymous referee (https://doi.org/10.5194/egusphere-2025-99-RC3) was the lack of synopticity in the dataset selected to evaluate the eddy's geometry and its derived properties—specifically, kinetic energy (KE), available potential energy (APE), available heat anomalies (AHA), and available salt anomalies (ASA).

Here, building on the framework proposed by Allen et al. [2001], we evaluate the degree of spatial distortion introduced during the sampling phase used for those calculations: the Oceanographic Transect (OceT) phase. The objective is to assess how accurately the eddy's true structure was captured under non-synoptic sampling conditions.

To this end, we compare the OceT results with quasi-synoptic sections that provide a more instantaneous view of the mesoscale structure. These comparisons, both visual and quantitative, help estimate the potential bias introduced by spatial distortion and are intended to directly address the methodological concerns raised during the review process.

## S1.1 Mathematical Formulation

Equation (10) from Allen et al. [2001] describes the effect of asynoptic sampling on the apparent wavelength of a propagating signal, as observed from a moving vessel:

$$\lambda' = \lambda \left(1 - \frac{c}{v_v}\right)^{-1} \tag{S1}$$

where:

- $\lambda$ is the true spatial wavelength of the feature (e.g. the intrinsic horizontal scale of the eddy),
- $c$ is the propagation speed of the feature (e.g., the eddy's translational velocity),
- $v_v$ is the vessel speed along the same axis as the feature's motion,
- $\lambda'$ is the apparent wavelength inferred from the moving platform.

This relationship captures a Doppler-like distortion introduced by the relative motion between the sampling platform and the moving feature. When the vessel travels in the same direction as the propagating feature ($c > 0$), the observed wavelength increases ($\lambda' > \lambda$); conversely, if the vessel moves against the propagation direction, the observed wavelength is shortened ($\lambda' < \lambda$). This Doppler-induced deformation can significantly affect the interpretation of mesoscale features, particularly when diagnosing their spatial structure or computing derived quantities that depend on horizontal gradients.

To formalize this distortion, we define a **Doppler Factor** $D$:

$$D = 1 - \frac{c}{v_v^{(\parallel)}} \tag{S2}$$

where:

- $c > 0$ is the propagation speed of the feature, defined as positive in a fixed reference direction,
- $v_v^{(\parallel)}$ is the component of the vessel's velocity along the same direction.

Depending on the sign of $v_v^{(\parallel)}$, the Doppler Factor can take two regimes:

- $v_v^{(\parallel)} > 0$: vessel moves in the same direction as the propagating feature (downstream),
- $v_v^{(\parallel)} < 0$: vessel moves in the opposite direction (upstream).

The Doppler Factor modifies the apparent wavelength as:

$$\lambda' = \frac{\lambda}{D} = \lambda \left(1 - \frac{c}{v_v^{(\parallel)}}\right)^{-1} \tag{S3}$$

Thus:

**Downstream sampling:** $D < 1 \Rightarrow \lambda' > \lambda$. The structure appears elongated.

**Upstream sampling:** $D > 1 \Rightarrow \lambda' < \lambda$. The structure appears compressed.

## S1.2 Effective along-propagation velocity in cross-stream transects

In cases where the vessel traverses the feature along a path that is not aligned with its direction of propagation (e.g., a cross-stream transect), the vessel's effective speed in the direction of the feature's movement must be projected onto the propagation axis. As shown by Allen et al. [2001], this projection can be expressed as:

$$v_f = v_s \frac{S}{S + \Lambda} \tag{S4}$$

Where:

- $v_v$ is the vessel's speed along the actual sampling path (e.g., the cross-stream transect),
- $v_f \equiv v_v^{(\parallel)}$ is the effective component of the vessel's speed projected along the direction of the feature's propagation,
- $S$ is the track leg separation,
- $\Lambda$ is the length of each cross front leg of the vessel's track.

This expression allows us to convert a cross-stream transect velocity $v_v$ into an equivalent along-stream velocity $v_f$, which can then be inserted into the Doppler factor and apparent wavelength expressions defined previously.

In our specific case, the vessel executed a single, long transect nearly orthogonal to the direction of the eddy's propagation. This situation corresponds to the limit where the cross-track leg length $\Lambda$ is much greater than the leg separation $S$, i.e., $S \ll \Lambda$. Under this condition, the projection of the vessel's speed onto the eddy's propagation direction—used to compute the Doppler factor—can be expanded as follows.

Starting from the projection formula given by Eq. S4, we introduce the small parameter $\epsilon = \frac{S}{\Lambda} \ll 1$, and rewrite the expression as:

$$v_f = v_s \cdot \frac{\epsilon}{1+\epsilon}$$

Expanding in powers of $\epsilon$ yields:

$$v_f \approx v_v \cdot \left(\epsilon - \epsilon^2 + \epsilon^3 - \dots\right) = v_v \cdot \left(\frac{S}{\Lambda} - \left(\frac{S}{\Lambda}\right)^2 + \left(\frac{S}{\Lambda}\right)^3 - \dots\right)$$

Since $S \to 0$ in our case, this shows that:

$$v_f \to 0 \quad \Rightarrow \quad D = 1 - \frac{c}{v_f} \to -\infty$$

That is, the **effective along-propagation velocity becomes negligible**, which implies a **strong Doppler-like distortion** when computing apparent wavelengths from a cross-eddy transect. In this regime, the classical Doppler factor and gradient-based diagnostics must be interpreted with caution or corrected using time-adjusted spatial coordinates.

## S1.3 Description of the survey phases

### S1.3.1 eIMPACT OceT phase

The non-synoptic phase corresponds to the **eIMPACT OceT phase**, conducted between 19 and 28 November 2022. It consisted of a series of 26 oceanographic stations along a nearly zonal transect (OceT) that crossed the eddy from east to west (Figure S1). At each station, vertical profiles of CTD-O and VMADCP were obtained. The stations were spaced approximately 12.7 ± 2.8 km apart, and the profiles extended from the surface to a depth of around 1500 m.

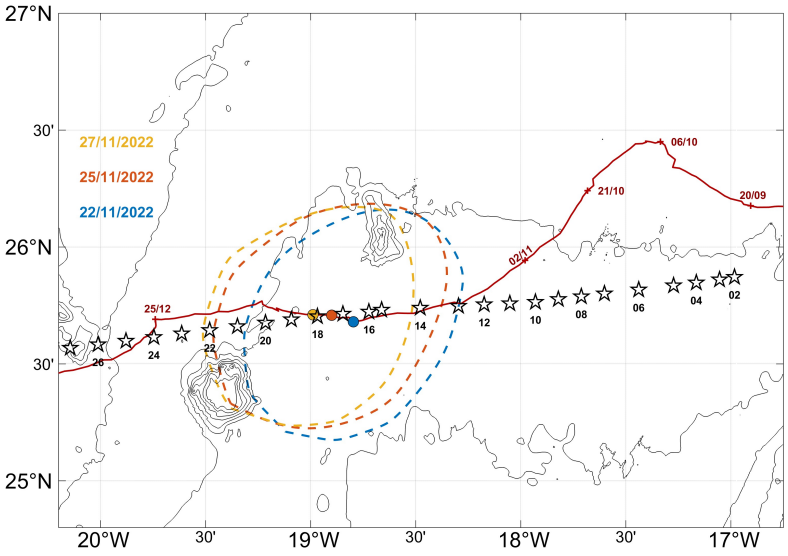


Figure S1: Study area showing the **eIMPACT OceT phase**. White stars indicate its 26 oceanographic stations. The thick dark red line traces the trajectory of the eddy with selected dates annotated. Colored dashed ellipses depict eddy's perimeter on specific days and corresponding colored dots mark its center.

As seen in Figure S1, some degree of distortion in the eddy's shape can be inferred from the sampling. This is explained by the fact that the Bentayga eddy was translating with an average velocity $c$ of $0.051 \pm 0.012$ m s$^{-1}$, while the R/V was moving in the same direction at a mean speed $v_v$ of $0.454 \pm 0.167$ m s$^{-1}$. As the anonymous referee pointed out, and as also discussed in Allen et al. [2001], this distortion resulting from the lack of synopticity may compromise the structural integrity of the eddy, introducing a significant bias in all calculations involving its spatial dimensions.

### S1.3.2 eIMPACT SeaSoar phase

The quasi-synoptic phase used in the main manuscript corresponds to the **eIMPACT SeaSoar phase**, conducted during 9–14 November 2022. Continuous measurements were obtained using a towed CTD-O mounted on an undulating SeaSoar vehicle, combined with VMADCP observations. This phase employed a southwest–northeast sampling grid consisting of seven transects (each approximately 278 km long), spaced by ∼22 km, and sampled vertical layers between 30 and 320 m depth (Figure S2). However, this dataset was primarily used to construct an objectively interpolated three-dimensional field, rather than to evaluate the structural shape of the Bentayga eddy.

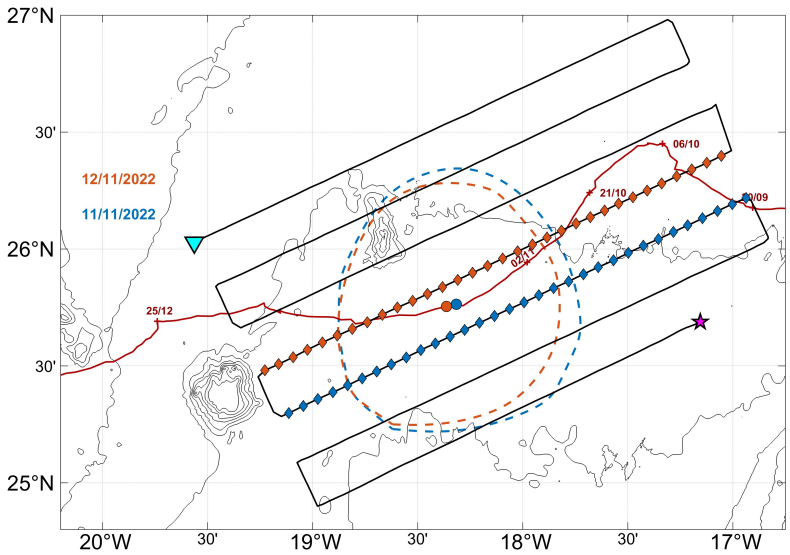


Figure S2: Same as Figure S1, but for the spatial coverage during the **eIMPACT SeaSoar phase**. Thick black lines indicate the grid-like trajectory of the R/V. Diamond markers highlight the paths of transects T3 and T4, both colored by date

In the present report, we use two of the seven along-eddy transects, selecting those closest to the eddy's center. For consistency, we retain their original numbering, with transect T3 located to the south and T4 to the north of the Bentayga eddy's center. Transect T3 was conducted on 11 November, approximately between 01:00 and 17:00 UTC, with the R/V moving in the same direction as the eddy at a mean velocity of $v_v = 4.31 \pm 0.092$ m s$^{-1}$, while the Bentayga eddy exhibited a translational velocity of $c = 0.041$ m s$^{-1}$. T4 was recorded between 19:00 UTC on 11 November and 10:00 UTC on 12 November, during which the R/V moved against the eddy's direction

at a speed of $v_v = 4.29 \pm 0.127$ m s$^{-1}$, while the eddy translated at a mean velocity of $c = 0.051 \pm 0.014$ m s$^{-1}$.

### S1.3.3 eIMPACT Ortho-transects phase

In addition to the main survey phases, a distinct configuration of two orthogonal transects—hereafter referred to as the **ortho-transects**—was conducted across the Bentayga eddy, forming a cross-shaped sampling pattern centered on the eddy (Figure S3). These transects were carried out immediately after the end of the **eIMPACT SeaSoar phase**, between 02:00 UTC on 14 November and 03:00 UTC on 15 November. During the **eIMPACT ortho-transects phase**, only VMADCP currents were continuously recorded. Since both transects intersected the eddy close to its center, they were used to evaluate the radial structure of its azimuthal velocities and to compare it with that obtained during the **eIMPACT OceT phase**.

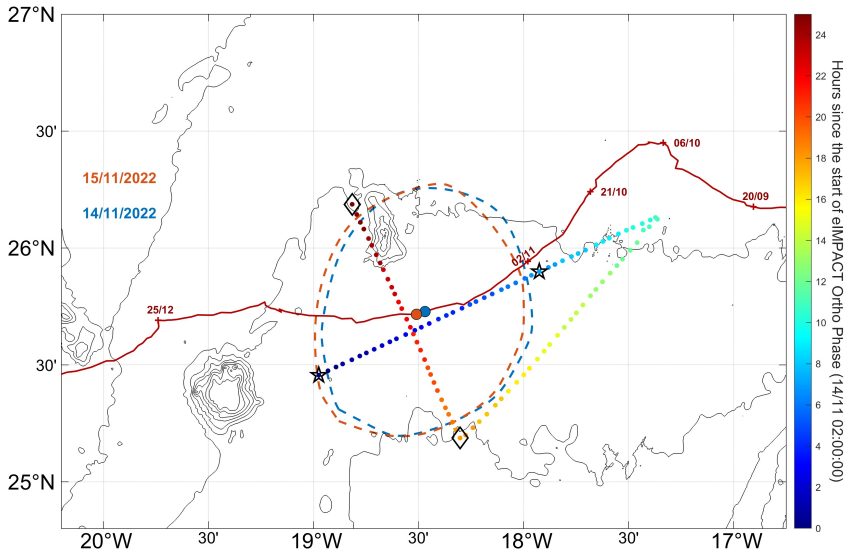


Figure S3: Same as Figure S1, but for the **eIMPACT ortho-transects phase**. The color-coded circles represent the full trajectory of the R/V, with colors indicating hours elapsed since the beginning of the phase (14 November at 02:00 UTC). Stars and diamonds mark the segments defining ZT and MT, which were selected for the analysis presented in this study.

The transects—hereafter named the Zonal Transect (ZT) and the Meridional Transect (MT)—crossed the eddy from west to east and from south to north, respectively. The ZT was conducted on 14 November 2022 between 02:00 and 08:00 UTC, spanning a total distance of 116.07 km. During this period, the R/V moved at an average speed ($v_v$) of 4.60 ± 0.22 m s$^{-1}$, opposite to the eddy's propagation direction, which exhibited a translational speed ($c$) of 0.0704 m s$^{-1}$. The MT was carried out between 19:00 UTC on 14 November and 03:00 UTC on 15 November, covering 122.43 km from south to north. In this case, the vessel moved at a similar speed of 4.66 ± 0.24 m s$^{-1}$, approximately orthogonal to the eddy's translational path.

## S1.4 Apparent Structure Deformation

### S1.4.1 OceT Transect: Along-Eddy Sampling

Based on the Doppler factor analysis presented above, we expect that the eddy structure observed during the **eIMPACT OceT phase** was subject to spatial distortion due to the asynoptic nature of the sampling. In particular, the Bentayga eddy translated westward at a mean speed of $c = 0.051 \pm 0.012\,\mathrm{m\ s^{-1}}$, while the R/V advanced in the same direction with a mean velocity of $v_v = 0.454 \pm 0.167\,\mathrm{m\ s^{-1}}$. Over the course of the ∼9-day transect, the eddy displaced approximately 40 km, a distance comparable to its inner-core radius (∼ 25 km) and substantial relative to its total horizontal scale (∼ 100 km). This motion is expected to stretch the apparent horizontal structure of the eddy in the direction of sampling, as predicted by the Doppler framework.

Figure 5 of the main manuscript—showing vertical sections of conservative temperature, absolute salinity, and potential density anomaly along OceT—presents signatures consistent with this elongation. In that study, however, we interpreted the structure as a physical feature of the eddy: an inner core surrounded by two distinct velocity rings, together spanning a radial width of ∼ 55 km. Interestingly, this scale is close to the mean displacement of the eddy during the OceT sampling phase, suggesting that the observed ring-like structure may, at least in part, result from Doppler-induced deformation.

As derived earlier, the Doppler Factor $D$ should quantify the distortion in the observed spatial scale due to asynoptic sampling. To express this distortion as a percentage change in the apparent spatial scale, we define:

$$\Delta_\lambda = \left( \frac{1}{D} - 1 \right) \times 100 \tag{S5}$$

Where:

- $\Delta_\lambda$ is the percentage of deformation in the apparent wavelength,
- $D = 1 - \frac{c}{v_v}$ is the Doppler Factor.

For the **eIMPACT OceT phase**, the eddy drift ($c$) and vessel speed ($v_v$) were:

$$c = 0.051 \pm 0.012\ \mathrm{m\ s^{-1}}, \qquad v_v = 0.454 \pm 0.167\ \mathrm{m\ s^{-1}}$$

This yields:

$$D = 1 - \frac{c}{v_v} = 1 - \frac{0.051}{0.454} \approx 0.888$$

Thus, the expected distortion is:

$$\Delta_\lambda = \left( \frac{1}{0.888} - 1 \right) \times 100 \approx 12.6\%$$

We can also estimate the uncertainty in $D$ given by:

$$\sigma_D = \left| \frac{\partial D}{\partial c} \right| \sigma_c + \left| \frac{\partial D}{\partial v_v} \right| \sigma_{v_v} = \left| -\frac{1}{v_v} \right| \sigma_c + \left| \frac{c}{v_v^2} \right| \sigma_{v_v} \tag{S6}$$

Then, inserting the numerical values:

$$\sigma_D = \left( \frac{1}{0.454} \cdot 0.012 \right) + \left( \frac{0.051}{(0.454)^2} \cdot 0.167 \right) \approx 0.026 + 0.023 = 0.049$$

To estimate the propagated uncertainty in $\Delta_\lambda$, we use:

$$\sigma_{\Delta_\lambda} = \left| \frac{d}{dD} \left( \frac{1}{D} - 1 \right) \times 100 \right| \cdot \sigma_D = \left( \frac{100}{D^2} \right) \cdot \sigma_D \tag{S7}$$

Yielding:

$$\sigma_{\Delta_\lambda} = \left( \frac{100}{0.888^2} \right) \cdot 0.049 \approx 126.8 \cdot 0.049 \approx 6.2\%$$

So, the sampling strategy during the **eIMPACT OceT phase** likely induced a spatial distortion of:

$$\Delta_\lambda = 12.6 \pm 6.2\%$$

Representing a non-negligible elongation of the apparent horizontal structure of the eddy, primarily along the sampling direction.

### S1.4.2 SeaSoar Transects T3 and T4: Opposing Sampling Directions

Transects T3 and T4 from the **eIMPACT SeaSoar phase** were conducted on consecutive days, representing contrasting sampling configurations: T3 was aligned with the eddy's propagation direction (downstream), while T4 was performed in the opposite direction (upstream).

**T3** was carried out on 11 November 2022, from 00:48 to 16:33 UTC, lasting approximately 15.8 hours. During this transect, the vessel advanced at a mean speed of $v_v = 4.314 \pm 0.092\,\mathrm{m\ s^{-1}}$, in the same direction as the Bentayga eddy, which translated at $c = 0.041\,\mathrm{m\ s^{-1}}$, moving approximately 2.33 km, which is minimal compared to its diameter ($\sim 100$ km). The Doppler factor was:

$$D = 1 - \frac{c}{v_v} = 1 - \frac{0.041}{4.314} \approx 0.9905$$

and the corresponding percentage of deformation:

$$\Delta_\lambda = \left( \frac{1}{D} - 1 \right) \times 100 \approx 0.96\%$$

To propagate the uncertainty:

$$\sigma_D = \left| \frac{\partial D}{\partial v_v} \right| \sigma_{v_v} = \left| \frac{c}{v_v^2} \right| \sigma_{v_v} = \left( \frac{0.041}{(4.314)^2} \right) \cdot 0.092 \approx 0.0002$$

$$\sigma_{\Delta_\lambda} = \left( \frac{100}{D^2} \right) \cdot \sigma_D = \left( \frac{100}{(0.9905)^2} \right) \cdot 0.0002 \approx 0.02\%$$

Thus:

$$\Delta_\lambda = 0.96 \pm 0.02\%$$

**T4** was conducted from 18:38 UTC on 11 November to 10:30 UTC on 12 November, with a duration of 15.9 hours. In this case, the vessel moved against the eddy's propagation direction at $v_v = 4.293 \pm 0.128\,\mathrm{m\ s^{-1}}$, while the Bentayga eddy translated at $c = 0.051\,\mathrm{m\ s^{-1}}$, displacing approximately 2.92 km during the transect. The resulting Doppler factor was:

$$D = 1 - \frac{c}{-v_v} = 1 + \frac{c}{v_v} = 1 + \frac{0.051}{4.293} \approx 1.0119$$

leading to:

$$\Delta_\lambda = \left(\frac{1}{D} - 1\right) \times 100 \approx -1.18\%$$

Uncertainty:

$$\sigma_D = \left(\frac{0.051}{(4.293)^2}\right) \cdot 0.128 \approx 0.0004$$

$$\sigma_{\Delta_\lambda} = \left(\frac{100}{D^2}\right) \cdot \sigma_D = \left(\frac{100}{(1.0119)^2}\right) \cdot 0.0004 \approx 0.039\%$$

Thus:

$$\Delta_\lambda = -1.18 \pm 0.04\%$$

Although T3 and T4 were performed with opposite orientations, both exhibit very small Doppler-induced deformation—less than 1.2%—with minor uncertainty. These results confirm that the SeaSoar transects can be considered quasi-synoptic, introducing negligible spatial distortion in the observed eddy structure.

### S1.4.3 ZT: Counter-Propagation Sampling

The Zonal Transect (ZT) of the **eIMPACT ortho-transects phase** was carried out on 14 November 2022, from 01:15 to 08:15 UTC, lasting approximately 7.0 hours. During this time, the vessel advanced nearly zonally in the opposite direction to the eddy's translation (i.e., upstream), at an average speed of $v_v = 4.604 \pm 0.223\,\mathrm{m\ s^{-1}}$, while the Bentayga eddy translated westward at $c = 0.070\,\mathrm{m\ s^{-1}}$.

Over the duration of the transect, the eddy displaced a horizontal distance of approximately 1.77 km. This displacement is relatively small compared to the transect length (116.07 km) and the horizontal scale of the eddy itself, indicating limited structural advection during the sampling.

The Doppler factor for this transect is:

$$D = 1 - \frac{c}{v_v} = 1 - \frac{0.070}{4.604} \approx 0.9848$$

The percentage of deformation in the apparent wavelength is then:

$$\Delta_\lambda = \left(\frac{1}{D} - 1\right) \times 100 \approx \left(\frac{1}{0.9848} - 1\right) \times 100 \approx 1.54\%$$

The uncertainty in $D$ is computed using first-order error propagation:

$$\sigma_D = \left|-\frac{1}{v_v}\right| \sigma_c + \left|\frac{c}{v_v^2}\right| \sigma_{v_v} = \frac{1}{4.604} \cdot 0.000 + \frac{0.070}{(4.604)^2} \cdot 0.223 \approx 0.00073$$

Then, the uncertainty in the percentage deformation becomes:

$$\sigma_{\Delta_\lambda} = \left(\frac{100}{D^2}\right) \cdot \sigma_D \approx \frac{100}{(0.9848)^2} \cdot 0.00073 \approx 0.075\%$$

Thus, the expected distortion due to asynoptic sampling during ZT is:

$$\Delta_\lambda = 1.54 \pm 0.08\%$$

This result confirms a negligible Doppler-induced deformation in the observed eddy structure. The short duration of the transect and the minimal displacement of the eddy—less than 2% of the transect length—further support the reliability of this section for analyzing the radial distribution of the eddy's azimuthal velocities.

### S1.4.4 MT: Cross-Propagation Sampling

Despite the theoretical sensitivity of cross-stream transects to asynoptic distortion, it is important to contextualize the impact in our specific case along MT. The eddy's translational velocity was relatively small, with $c = 0.0704\,\mathrm{m\ s^{-1}}$, while the R/V moved at an average speed of $v_v \approx 4.66\,\mathrm{m\ s^{-1}}$. The full cross-eddy transect (MT) lasted approximately 7.3 hours, during which the eddy displaced by only about 1.8 km. Given the eddy's horizontal scale—exceeding 100 km in diameter—this displacement is minor and unlikely to produce a significant distortion in the inferred structure.

Moreover, while the rotational motion of fluid parcels could also contribute to internal distortion, results from the main manuscript show that the azimuthal velocities in the inner core (within a radius of $\sim$ 25 km) result in rotation periods of approximately 4 days. Since this rotational timescale is significantly longer than the duration of the MT transect, the relative motion of water parcels during the sampling window is minimal. Additionally, this rotational period increases with radius, further reducing the likelihood of substantial deformation at larger distances from the eddy center.

Therefore, although the theoretical framework suggests a strong potential for Doppler-like distortion in cross-stream transects, both the slow drift of the eddy and the relatively slow internal rotation imply that, in our case, the effect is likely to be small. This supports the validity of using MT to compare the radial structure of azimuthal velocities, as theoretical considerations suggest that asynoptic distortions should be limited in this case.

Table S1: Summary of Doppler distortion analysis for the different sampling phases. For each transect, we show the direction of sampling relative to the eddy's propagation, average vessel speed ($v_v$), mean eddy translation speed ($c$), total duration ($\Delta t$), eddy displacement during sampling ($\Delta x$), Doppler Factor ($D$), and the estimated deformation in observed wavelength ($\Delta_\lambda$).

| **Transect** | **Direction** | $v_v$ [m/s] | $c$ [m/s] | $\Delta t$ | $\Delta x$ [km] | $D$ | $\Delta_\lambda$ [%] |
|---|---|---|---|---|---|---|---|
| OceT | Downstream | 0.454 | 0.051 | 9.0 d | 40.0 | $0.888 \pm 0.049$ | $12.6 \pm 6.2$ |
| T3 | Downstream | 4.314 | 0.041 | 15.8 h | 2.33 | $0.990 \pm 0.002$ | $1.0 \pm 0.2$ |
| T4 | Upstream | 4.293 | 0.051 | 15.9 h | 2.92 | $1.012 \pm 0.003$ | $-1.2 \pm 0.3$ |
| ZT | Upstream | 4.604 | 0.070 | 7.0 h | 1.77 | $1.015 \pm 0.005$ | $-1.5 \pm 0.5$ |
| MT | Orthogonal | 4.662 | 0.070 | 7.3 h | 1.84 | — | — |

To summarize the results presented throughout this section, Table S1 compiles the key parameters used in the Doppler distortion analysis for each sampling transect. The table includes the direction of sampling relative to the eddy's propagation, the average vessel and eddy speeds, total sampling duration, the eddy's displacement during each transect, and the corresponding Doppler factor and wavelength deformation. This synthesis allows for a direct comparison of the magnitude of Doppler-like effects across phases. Notably, the strongest deformation is associated with the eIMPACT OceT phase, where the eddy's slow but sustained displacement over nine days likely contributed to a non-negligible spatial bias. In contrast, transects T3, T4, and ZT exhibit minimal deformation, reinforcing their value as quasi-synoptic references. Although Doppler metrics were not formally computed for MT due to its orthogonal orientation, our earlier discussion supports its

reliability as a reference transect given the minimal eddy movement and slow internal rotation during its sampling.

# S2: Idealized eddy reconstruction from quasi-synoptic sections

## S2.1 Raw hydrographic structure along T3 and T4

The SeaSoar transects T3 and T4 were conducted during the eIMPACT2 survey between 11 and 12 November 2022. Both sections crossed the Bentayga eddy along near-parallel paths, slightly offset from its geometric center—T3 sampling the southern region and T4 the northern. The undulating SeaSoar platform profiled the upper ocean (30–320 m depth) with a vertical resolution of approximately 2 m and a horizontal resolution of 1.5 km.

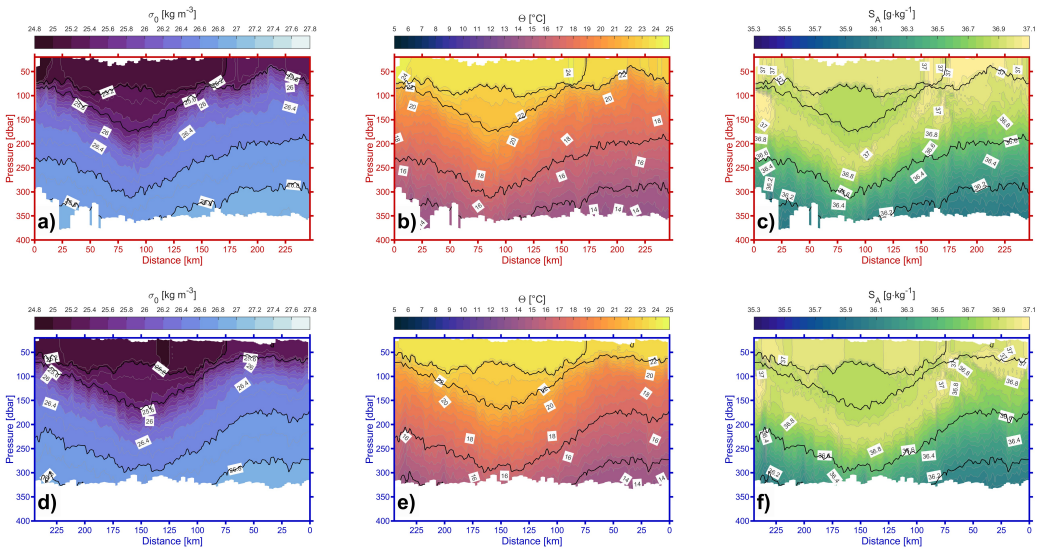


Figure S4: Vertical sections of (a,d) potential density anomaly ($\sigma_\theta$), (b,e) conservative temperature ($\Theta$), and (c,f) absolute salinity ($S_A$) for transects T4 (top row) and T3 (bottom row). The distance axis is defined along the transect track, with pressure as the vertical coordinate. Data were collected using the SeaSoar platform during the eIMPACT2 survey.

Figure S4 presents vertical sections of potential density anomaly ($\sigma_\theta$), conservative temperature ($\Theta$), and absolute salinity ($S_A$) along T4 (upper panels) and T3 (lower panels). These profiles reveal the internal hydrographic structure of the eddy and provide a reference for evaluating its spatial symmetry and vertical stratification. These quasi-synoptic observations are central to the ongoing effort to assess the potential spatial distortion introduced by the non-synoptic sampling performed during the OceT phase.

In particular, they are being used to construct an idealized radial representation of the eddy, which serves as a baseline for comparison against the potentially deformed patterns observed in OceT. This reconstruction is being approached by interpolating the hydrographic properties from T3 and T4 onto a common radial coordinate system centered on the estimated eddy core. Each data point is assigned a radial distance from this center, enabling the aggregation of values into a smoothed, azimuthally symmetric structure. The resulting fields aim to represent a reference eddy minimally affected by

Doppler-like distortion, against which the features observed in OceT can be contrasted. This process is intended to help disentangle genuine physical asymmetries from sampling-induced artifacts and to clarify whether features such as elongation or displaced cores are intrinsic or methodological in origin.

## S2.2 Reconstruction

To construct a synoptically consistent, azimuthally averaged representation of the Bentayga eddy, we developed an objective mapping framework that merges the quasi-parallel hydrographic sections T3 and T4. Although neither transect intersected the eddy centroid precisely, both exhibited coherent thermohaline anomalies consistent with a symmetric intrathermocline vortex. This approach, grounded in the assumption of radial symmetry, provides a reference eddy structure that is minimally affected by sampling artifacts.

First, the eddy center in each transect was identified as the location where the vertical distance between the 26.2 and 26.5 kg $m^{-3}$ isopycnals reached a maximum. These isopycnals delineate the upper and lower boundaries of the quasi-homogeneous intrathermocline core of the Bentayga eddy. The spatial offset between the inferred eddy centers in T3 and T4 was decomposed into components parallel and perpendicular to the mean transect orientation. Using a right-triangle approximation and accounting for the local radius of curvature, we projected the T4 transect horizontally onto the axis of T3, thereby aligning the inferred eddy cores in geographic space. All coordinate transformations were performed in spherical geometry, with distances in kilometers converted to degrees of latitude and longitude using the WGS84 ellipsoid.

Once aligned, the transects were rotated to a common orientation (mean angle $\bar{\theta} = 67.1°$) and interpolated onto a reference grid centered at the eddy core as inferred from T3. An anisotropic Gaussian covariance model was then used to perform objective interpolation of each hydrographic variable. The covariance function was defined as:

$$C(x, y) = \varepsilon\delta(x, y) + (1 - \varepsilon) \exp\left[-\left(\frac{x^2}{L_x^2} + \frac{y^2}{L_y^2}\right)\right], \tag{S8}$$

where $x$ and $y$ are rotated distances along and across the transect, $L_x$ and $L_y$ are the horizontal decorrelation scales (here both set to 33 km), $\varepsilon$ is the relative measurement error variance (5%), and $\delta(x, y)$ is the Dirac delta function. The values of $L_x$ and $L_y$ were estimated empirically as the integral length scale, calculated from the area under the spatial cross-correlation function of $\sigma_\theta$ anomalies between the two transects at 115 dbar, a depth near the eddy's maximum azimuthal velocity.

The objectively mapped fields were projected onto a radial transect intersecting the eddy center, resulting in an idealized cross-section that preserves the dominant hydrographic gradients while mitigating distortions introduced by the angular separation and temporal lag of the original observational transects. This representation—referred to as the asymmetric idealized eddy—reveals a clear radial asymmetry, particularly in the shape and extent of the core structure (Figure S5a-c). To further examine this asymmetry, a symmetric counterpart was constructed by computing the radial mean of the hydrographic properties and reflecting the structure about the eddy centerline, effectively generating a mirror image with a vertical nodal axis (Figure S5d-f). This symmetric version serves as a baseline for evaluating the spatial distortions present in the original eddy geometry.

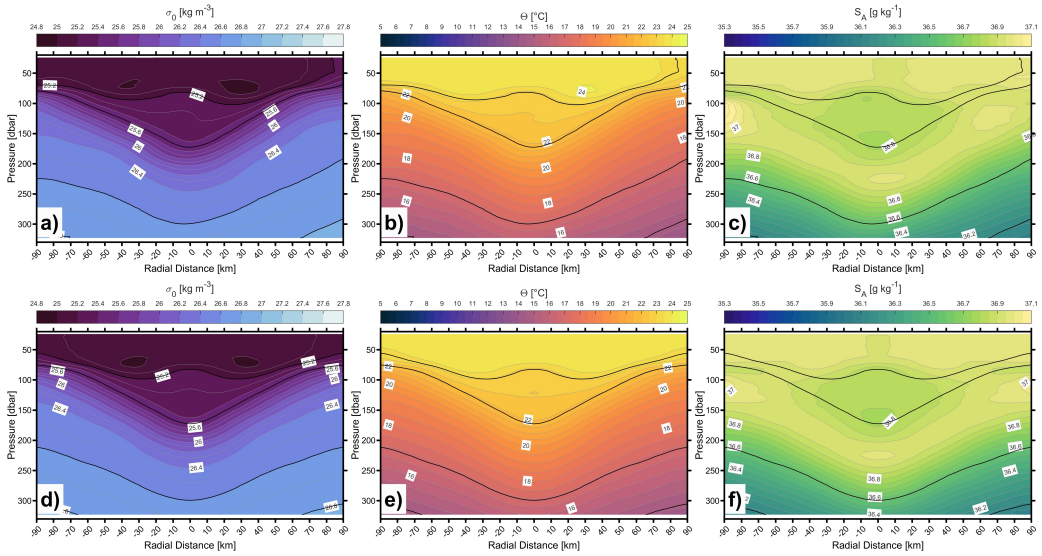


Figure S5: Vertical sections of (a,d) potential density anomaly ($\sigma_\theta$), (b,e) conservative temperature ($\Theta$), and (c,f) absolute salinity ($S_A$) for the smoothed asymmetric (top row) and symmetric idealized eddy (bottom row). The distance axis is defined as a radial distance from its center, with pressure as the vertical coordinate.

## S2.3 Eddy Asymmetry

Figure S6 illustrates the asymmetry of the Bentayga eddy through the radial distribution of its upper and lower boundaries, represented by the depths of the 25.2 and 25.5 kg m$^{-3}$ isopycnals, respectively. A comparison between the asymmetric and symmetric eddy structures reveals that both isopycnals reach greater depths on the western flank of the asymmetric eddy (negative radial distances), beginning around 40 km and 25 km from the eddy center for the upper and lower isopycnals, respectively. Conversely, on the eastern flank, the isopycnals tend to lie slightly shallower than in the symmetric counterpart, with the deviation starting at radial distances comparable to those on the western side (Figure S6a). This pattern underscores a pronounced west–east asymmetry and a vertical imbalance between the upper and lower halves of the Bentayga eddy.

Figure S6b quantifies this vertical displacement by showing the depth difference between the two eddy configurations for each isopycnal. Positive values indicate that the isopycnal in the asymmetric eddy lies deeper than in the symmetric counterpart, while negative values denote a shallower position. The 25.2 kg m$^{-3}$ isopycnal exhibits deviation amplitudes ranging from 3 to 7 m within radial distances of approximately ±80 km from the eddy center. Within the core region (±40 km), these deviations are notably larger than those observed in the 25.5 kg m$^{-3}$ isopycnal, which remain within $\leq$3 m. However, beyond 40 km, the 25.5 kg m$^{-3}$ isopycnal shows increased deviations, reaching amplitudes of 5–8 m near 80 km. This pattern suggests a subtle tilting of the eddy's upper structure, while the lower layers remain more vertically aligned, exhibiting a higher degree of symmetry around ±25 km from the eddy center. Overall, these results highlight a distinct vertical asymmetry concentrated in the upper portion of the eddy core, likely resulting from lateral stirring or uneven hydrographic preconditioning during the eddy's formation.

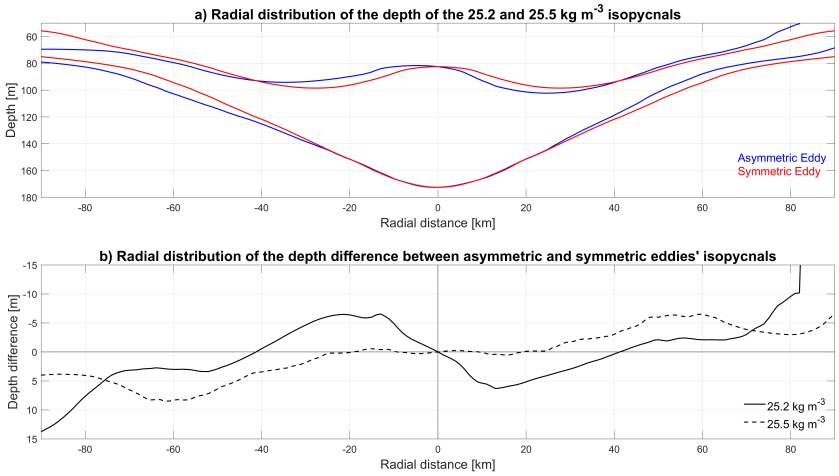


Figure S6: (a) Radial distribution of the depth of the 25.2 and 25.5 kg m$^{-3}$ isopycnals for the asymmetric (blue) and symmetric (red) eddy representations. (b) Depth difference between the two eddy structures, calculated as asymmetric minus symmetric. Positive (negative) values indicate a deeper (shallower) isopycnal in the asymmetric eddy.

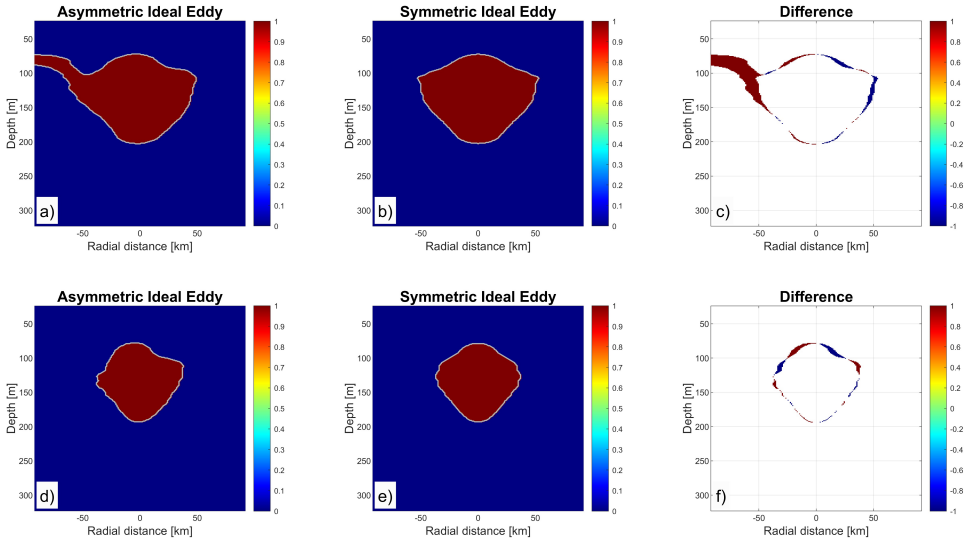


Figure S7: Panels (a)–(c) and (d)–(f) show the spatial extent of the 36.9 and 36.85 g kg$^{-1}$ isohalines, respectively, which characterize the core of the Bentayga eddy. The left and middle columns display the asymmetric and symmetric idealized versions of the eddy, respectively. The right column presents the signed difference (*asymmetric minus symmetric*), where red and blue colors indicate regions of expansion and contraction, respectively.

Figure S7 characterizes the morphological asymmetry of the Bentayga eddy based on the horizontal extent of its core, as delineated by the 36.9 and 36.85 g kg$^{-1}$ isohalines. These surfaces capture the salinity envelope associated with the eddy's quasi-homogeneous core. The structure defined by the 36.9 g kg$^{-1}$ isohaline (Figure S7a–c) reveals a prominent west–east asymmetry, with the eddy's western flank extending ra-

dially farther than its eastern counterpart. This broader spatial footprint near the core coincides with a flattened outer rim that transitions into a vertically elongated center. A distinctive salinity-rich feature extends from the eddy's northwestern quadrant, suggesting the presence of a tongue-like intrusion that may reflect isopycnal water mass exchange or the partial entrainment of an external remnant filament. In contrast, the eastern flank appears more compact in its radial extent, although vertically it remains comparable.

The asymmetry becomes even more evident in the upper layers of the eddy when examined through the 36.85 g $kg^{-1}$ isohaline (Figure S7d–f), which outlines a slightly smaller region than the 36.9 g $kg^{-1}$ isohaline. Notably, this shallower salinity surface reveals greater structural deviations above 100 m depth. The upper boundary of the eddy exhibits a clear tilt, whereas the lower boundary remains relatively symmetric. Consistent with the pattern depicted by the bounding isopycnals, these findings suggest that deviations from radial symmetry are most pronounced near the eddy's upper boundary, where interactions with surrounding waters and surface forcing are more dynamically active. The 36.9 g $kg^{-1}$ isohaline, in contrast, seems to capture the interface between the eddy core and its surrounding rim, functioning as a transition layer between well-mixed interior waters and ambient hydrography.

To quantify these morphological deviations, we computed the net areal difference between the regions enclosed by the 36.85 g $kg^{-1}$ isohaline in the asymmetric and symmetric eddy representations. The total discrepancy was modest, yielding a net difference of just 0.21% relative to the symmetric structure's area. However, a directional breakdown of these deviations revealed that the asymmetric eddy enclosed a 3.91% smaller area in certain regions, indicating local contraction, and a 4.11% larger area in others, indicating localized expansion. These near-compensating values underscore that while the eddy's total volume remains nearly conserved, its internal structure is reorganized in a markedly asymmetric fashion—extending farther westward while being slightly compressed on the eastern flank.

# S3: Radial zonation based on hydrographic and velocity structure

In search of a robust criterion to delineate the radial extent influenced by the hydrographic and dynamical properties of the Bentayga eddy, we present an adapted methodology based on the analysis of Bosse et al. [2018, 2019].

## S3.1 Hydrographic constraints across the Bentayga eddy core

Figure S8 displays the radial distribution of hydrographic properties between 85 and 165 m depth, relative to the eddy center. This depth interval corresponds to the vertical range where the eddy core is best defined in terms of quasi-homogeneous hydrography ($\overline{\sigma_0}$ = 25.3±0.05 kg m$^{-3}$, $\overline{\Theta}$ = 22.5±0.2 °C, and $\overline{S_A}$ = 36.83±0.01 g kg$^{-1}$), as previously identified in the vertical sections. The objective of this analysis is to evaluate the radial gradients of three key variables—$\sigma_0$, $\Theta$, and $S_A$—to determine a physically grounded zonation of the Bentayga eddy. Each panel in Figure S8 contrasts three representations: the full set of individual observations (from both the eIMPACT SeaSoar and OceT phases), the bin-averaged radial profiles, and the radial structures extracted from the idealized eddy transects (both asymmetric and symmetric configurations at 115 m depth).

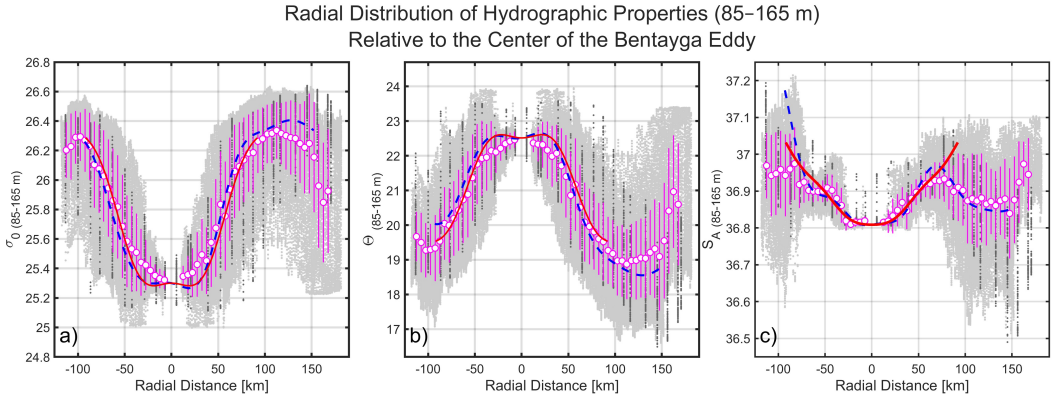


Figure S8: Radial distribution of hydrographic properties between 85 and 165 m depth relative to the center of the Bentayga eddy. Panels show: (a) potential density anomaly ($\sigma_0$), (b) conservative temperature ($\Theta$), and (c) absolute salinity ($S_A$). Light gray points correspond to data collected during the eIMPACT SeaSoar phase, and dark gray points represent profiles obtained during the OceT phase. White circles with magenta edges denote 5-km radial means computed from the combined SeaSoar and OceT datasets; error bars indicate ±1 standard deviation and are shown only when more than 100 data points were available within a given bin. The dashed blue and solid red lines represent the radial structure at 115 m depth extracted from the asymmetric and symmetric idealized eddy transects, respectively.

All three variables exhibit coherent radial gradients consistent with a canonical core, ring, and background eddy structure. For $\sigma_0$ (Figure S8a), a pronounced bowl-shaped

anomaly is centered around 0 km, with a minimum near 25.3 $\mathrm{kg\,m^{-3}}$. Density increases steeply starting at 40-50 km from the eddy center, approaching background values beyond approximately 80 km. Conservative temperature ($\Theta$; Figure S8b) and absolute salinity ($S_A$; Figure S8c) display inverse patterns relative to density, characterized by elevated temperatures and reduced salinities at the eddy center. Both variables transition toward ambient values with increasing radial distance, although their gradients differ: temperature exhibits a broader transition zone (from approximately 40 to 80 km away from the eddy center), while salinity presents a sharper core–ring contrast. These differences underscore the role of salinity as the dominant contributor to the eddy core structure at this depth range.

The bin-averaged profiles (white circles with magenta edges) effectively suppress small-scale noise and enhance the mesoscale signal of the eddy's hydrographic structure. These profiles qualitatively match the asymmetric idealized eddy (dashed blue lines), particularly within the inner 40 km for $S_A$ and across the radial range outside ± 40 km for both $\sigma_0$ and $\Theta$. In contrast, the symmetric eddy profiles (solid red lines) replicate the general radial architecture but fail to capture observed asymmetries and sharper gradients, most notably in salinity (beyond 50 km). Among the three variables, $S_A$ provides the most consistent depiction of the eddy core, exhibiting minimal internal variability and strong agreement among observed, binned, and idealized profiles. While $\sigma_0$ delineates the broader core–ring transition, salinity most clearly defines the extent and sharpness of the core–background interface. Temperature, though coherent, exhibits as $\sigma_0$ a broader transition and greater variability beyond the core.

To define radial zones within the Bentayga eddy, we examine the variability of $S_A$, which displays the most compact and radially homogeneous core structure among the three hydrographic variables. Within a radial distance of approximately ±23 km from the eddy center, $S_A$ shows minimal internal variability (mean salinity 36.82±0.007 $\mathrm{g\,kg^{-1}}$), with strong consistency across both observational and idealized profiles (mean deviations of ∼0.003 $\mathrm{g\,kg^{-1}}$). This region is thus identified as the well-mixed eddy core. Between 23 and 40 km, the salinity distribution displays increasing dispersion (0.02–0.05 $\mathrm{g\,kg^{-1}}$), corresponding to a transition/rim zone, defining the surrounding ring. Beyond 40 km, variability intensifies (0.03–0.13 $\mathrm{g\,kg^{-1}}$), and radial gradients weaken (±0.003 $\mathrm{g\,kg^{-1}}$), indicating the transition into the ambient background environment.

## S3.2 Kinematic zonation and dynamical behavior of eddy

We also analyzed the radial distribution of observed azimuthal velocities ($v_\theta$) within the 80–160 m depth range, which corresponds to the core layer of the Bentayga eddy (Figure S9a). As anticipated, the velocity profiles exhibit a degree of radial asymmetry; however, they remain remarkably consistent across the different observational phases. This asymmetry becomes more evident beyond the radius of the well-mixed core ($|r| > R_c = 23$ km), within which the profiles display a near-linear increase in $v_\theta$ consistent with solid-body rotation. Outside this core region, azimuthal velocities continue to increase, albeit more gradually, reaching their maximum at approximately 35–40 km from the eddy center. Beyond this point, $v_\theta$ progressively decreases, following a pattern similar to the decay observed in Gaussian-like vortex structures. This radial behavior suggests that the eddy's dynamical profile transitions from a Rankine-type structure near the core to a more Gaussian-like distribution in the surrounding ring.

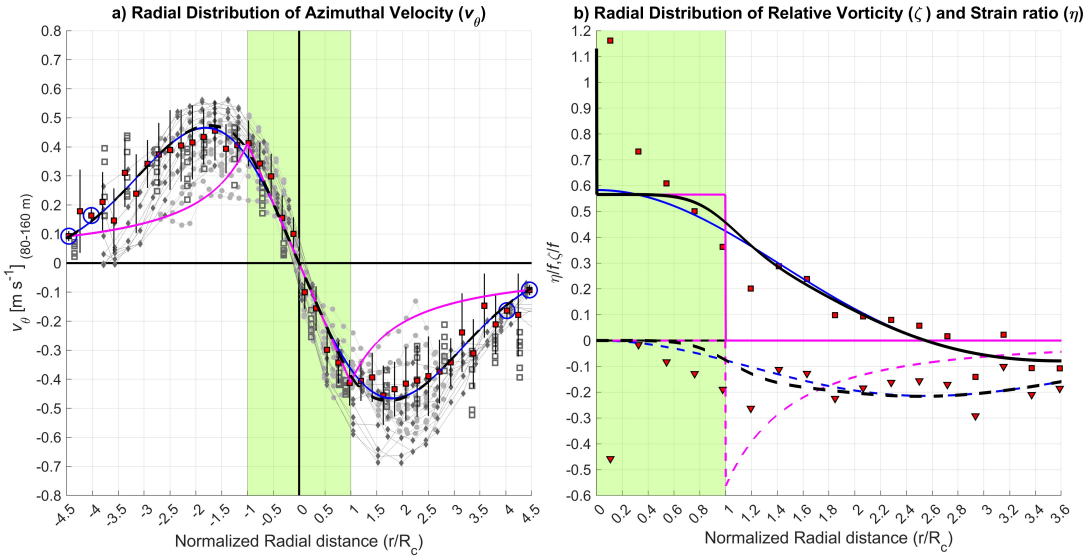


Figure S9: a) Radial distribution of azimuthal velocity ($v_\theta$) between 80 and 160 m depth, relative to the center of the Bentayga eddy. Gray markers represent individual measurements from different survey phases: SeaSoar (T3 and T4; dark gray diamonds), Orthotransects (ZT and MT; light gray circles), and OceT (dark gray open squares). The binned mean profile is shown as red-filled black squares, calculated over 5-km radial intervals; vertical bars indicate $\pm 1$ standard deviation. Blue-circled markers highlight bins with fewer than 10 observations. Model-derived velocity profiles are overlaid: Rankine vortex (magenta), Gaussian vortex (blue), and the hybrid smoothed transition (black dashed). b) Normalized relative vorticity ($\zeta/f$, squares and solid lines) and strain rate ($\eta/f$, triangles and dashed lines) as a function of normalized radial distance. Symbols denote observed values, and curves follow the same color scheme as in panel a). The green-shaded region in both panels marks the extent of the well-mixed eddy core ($|r| \leq R_c = 23$ km).

To further explore this hypothesis, Figure S9a also presents the theoretical azimuthal velocity profiles corresponding to two classical vortex models across the studied radial domain. For the Rankine vortex, the azimuthal velocity (${v_\theta}^R(r)$) was computed using the observed $R_c$ as the transition radius between the solid-body rotation and the outer hyperbolic decay, with a peak velocity $v_{max} = 40 \pm 8$ cm s$^{-1}$, estimated from the average value of $v_\theta$ at $R_c$ (see red squares in Figure S9a):

$$ {v_\theta}^R(r) = \begin{cases} v_{max} \dfrac{r}{R_c}, & \text{for } r \leq R_c \\ v_{max} \dfrac{R_c}{r}, & \text{for } r > R_c \end{cases} \tag{S9} $$

The Gaussian-like vortex profile (${v_\theta}^G(r)$) was derived through a least-squares fitting of the form:

$$ {v_\theta}^G(r) = v_{max} \frac{r}{R_m} \exp\left[\frac{1}{2}\left(1 - \left(\frac{r}{R_m}\right)^2\right)\right] \tag{S10} $$

with $v_{max} = 46$ cm s$^{-1}$ and a maximum velocity radius of $R_m = 41$ km. Both theoretical curves show reasonable agreement with the observations over the respective radial ranges, supporting the notion of a mixed dynamical regime within the eddy. The transition

between the two regimes appears to occur between approximately $R_c$ and $1.6R_c$. To model this transition, a hybrid formulation (${v_\theta}^{HS}(r)$) was introduced by smoothly combining the Rankine and Gaussian profiles using a logistic weighting function $w(r)$:

$$w(r) = \frac{1}{1 + \exp\left[-k(r - R_c)\right]} \tag{S11}$$

$${v_\theta}^{HS}(r) = (1 - w(r)) \cdot {v_\theta}^{R}(r) + w(r) \cdot {v_\theta}^{G}(r) \tag{S12}$$

where $k = 0.2$ defines the steepness of the transition. This hybrid model preserves the solid-body rotation characteristic of the well-mixed eddy core ($|r| \leq R_c$), while gradually transitioning to the Gaussian-like increase and decay observed in the surrounding ring ($R_c \leq |r| \leq 3R_c \approx 70$ km). This formulation captures the average dynamical structure of the Bentayga eddy, including its peripheral variability, while providing a consistent analytical approximation.

We also analyzed the radial structure of relative vorticity ($\zeta$) and strain ratio ($\eta$), computed from the azimuthal velocity field $v_\theta(r)$. Assuming axisymmetry and positive radial distance ($r$), the quantities were evaluated using their polar coordinate formulations:

$$\zeta(r) = \frac{1}{r} \cdot \frac{d}{dr}\left[r \cdot v_\theta(r)\right] \tag{S13}$$

$$\eta(r) = \frac{dv_\theta}{dr} - \frac{v_\theta}{r} \tag{S14}$$

Here, $\zeta$ represents the flow's rotational component, while $\eta$ characterizes the azimuthal shear deformation. Numerical derivatives were computed over uniformly spaced radial bins, and both quantities were normalized by the local Coriolis parameter ($f$) to enable dynamical interpretation.

Figure S9b displays the resulting normalized profiles of $\zeta/f$ and $\eta/f$, derived from observations along with the corresponding theoretical curves from the Rankine, Gaussian, and hybrid vortex models. In general, the observed vorticity profile aligns well with the theoretical expectations, especially within the surrounding ring region ($R_c \leq |r| \leq 3R_c$). Inside the well-mixed eddy core ($|r| \leq R_c$), the observed $\zeta/f$ remains approximately constant—consistent with solid-body rotation—but exhibits a modest increase toward the eddy center. This deviation likely reflects enhanced sensitivity to noise near $r = 0$, limited spatial resolution, and slight nonlinearity in the observed velocity field. In contrast, the observed strain ratio profile displays more irregular behavior and deviates significantly from the theoretical predictions. While the hybrid model captures the expected radial decay of $\eta/f$, the observed values exhibit high variability and reduced amplitude. These discrepancies may stem from a combination of observational noise, radial asymmetries, and the simplifications inherent in the derivation of Eq. S14, which assumes perfectly circular flow. Internal deformation processes such as filamentation or submesoscale instabilities could also introduce local strain anomalies not captured by the idealized vortex models [Brannigan et al., 2017; Thomas et al., 2013]. Despite these limitations, the hybrid model serves as a useful first-order approximation that captures the dominant rotational and shear features of the Bentayga eddy.

From this combined hydrographic–kinematic perspective, the Bentayga eddy exhibits a radially stratified structure that broadly aligns with classical vortex theory, while revealing key observational refinements. The innermost region, extending up to $R_c \approx 23$ km, defines a quasi-homogeneous core where the variance of $S_A$ is minimal and azimuthal velocity increases linearly with radius—hallmarks of a Rankine-type solid-body rotation

regime. This layer appears dynamically stable and internally coherent across independent observational phases, supporting its interpretation as the well-mixed eddy core. Between $R_c$ and $R_e = 3R_c \approx 70$ km, we identify a surrounding ring characterized by intensified radial salinity gradients and a Gaussian-like azimuthal velocity distribution that peaks near $R_m \sim 41$ km. This region marks a dynamical transition, with decreasing relative vorticity and increasing strain rate—indicative of enhanced deformation and incipient coupling with ambient waters. The coherence between the hybrid vortex model and observed velocity profiles across this band supports the use of $R_e$ as the outer limit of the eddy's dynamical influence. Beyond $R_e$, velocity amplitudes and hydrographic gradients decline substantially, and the signal of the eddy structure becomes indistinguishable from the background environment. These empirically constrained radial zones—core, surrounding ring, and background—provide a physically grounded framework for subsequent integrations of eddy properties, including energy content, thermohaline anomalies, and lateral transport estimates.

# S4: Sensitivity of integrated budgets to domain boundaries

Quantifying the energy content and hydrographic anomalies of mesoscale eddies requires a physically consistent definition of the integration domain. For the Bentayga eddy, radial boundaries are defined based on the coherence of hydrographic properties and azimuthal velocity profiles, delineating a well-mixed core ($|r| \leq R_c$) and a broader surrounding ring ($R_c < |r| \leq R_e$). Vertical boundaries are more challenging to set and may depend on criteria such as the persistence of anomalies, isopycnal displacements, nonlinearity conditions ($U/c > 1$), or data availability. We evaluate kinetic energy (KE), available potential energy (APE), and integrated available heat (AHA) and salt (ASA) anomalies. All estimates are derived using empirically defined spatial limits, comparing observational (OceT) and idealized (symmetric and asymmetric) eddy representations. Radial integration limits ($R_{\text{upper}}$) span 20–75 km (1 km increments), while vertical integration domains vary according to data availability: KE is evaluated from −550 to −40 m (VMADCP range), and APE, AHA, and ASA are integrated between −337 and −14 m, matching the idealized eddy data range.

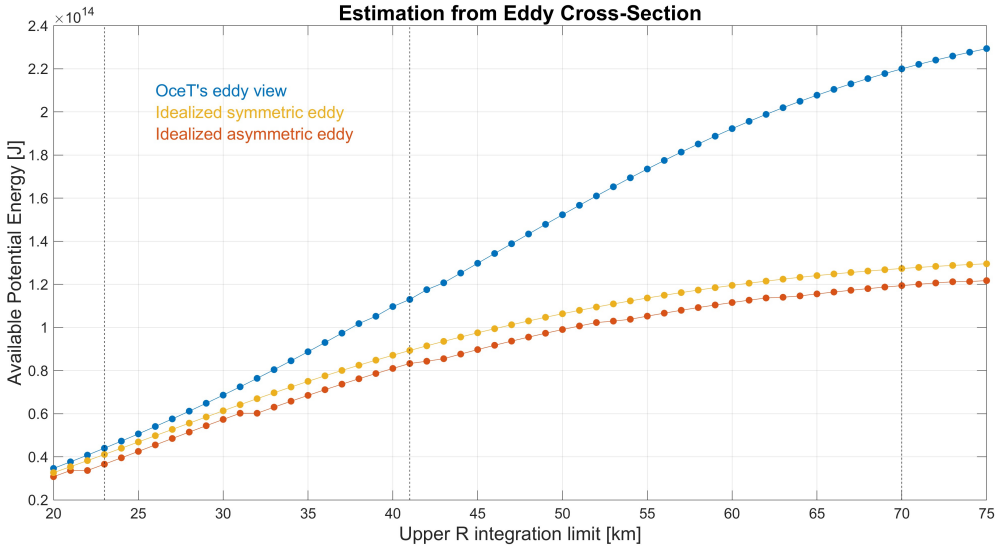


Figure S10: Sensitivity of Available Potential Energy (APE) estimates to variations in the radial integration limit ($R_{\text{upper}}$). APE was calculated using the observationally derived OceT view (blue), the idealized symmetric eddy (yellow), and the idealized asymmetric eddy (red). All estimates were integrated over a fixed vertical domain spanning from -337 m to -14 m. Dashed vertical lines indicate reference radial limits associated with key structural radii: the edge of the well-mixed core ($R_c = 23$ km), the radius of maximum azimuthal velocity ($R_m \approx 41$ km), and the outer boundary of the surrounding ring ($R_e = 70$ km).

APE is first analyzed with respect to radial integration. As shown in the Figure S10, APE estimates from the OceT section align well with those from idealized eddies within the eddy core ($R_{\text{upper}} \leq 23$ km, ∼6.5% difference). Discrepancies increase outward, exceeding 40% at $R_{\text{upper}} = 70$km, due to structural variability and observational distortion. Figure S11 complements this by analyzing vertical integration sensitivity. Limiting in-

tegration to −337 m results in underestimations of 20–22%, most pronounced beyond $R = 41$ km.

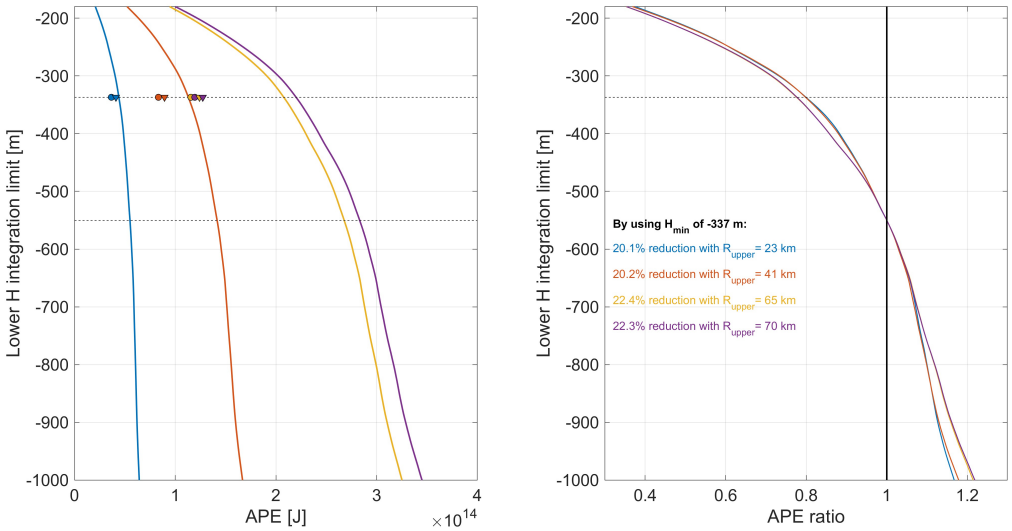


Figure S11: Sensitivity of APE estimates to vertical integration limits using the OceT dataset. Left: APE as a function of the lower integration boundary ($H_{\min}$) for four radial domains: $R_{\text{upper}} = 23$ km (blue), 41 km (red), 65 km (orange), and 70 km (violet). Circle and triangle markers denote values computed from the idealized asymmetric and symmetric eddy sections, respectively. Dashed lines mark vertical limits of −337 m and −550 m used in prior estimates. Right: APE ratios normalized by the value obtained with $H_{\min} = -550$ m.

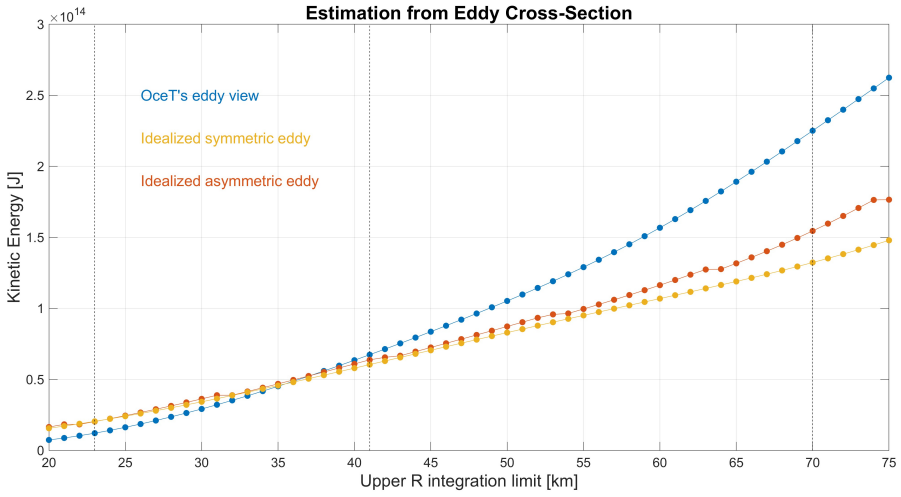


Figure S12: Same as Figure S10 but for the integrated kinetic energy (KE) of the Bentayga eddy. In this case the vertical integration range is fixed from the surface down to $z = -550$ m.

Figure S12 shows radial sensitivity of KE. KE increases with $R_{\text{upper}}$, with good agreement ($< 10\%$) across all representations within 30 km. Beyond this, OceT values diverge

due to the high sensitivity of KE to asymmetric and localized velocity enhancements, and temporal-spatial distortions in the OceT section. Idealized eddies assume axisymmetry, underestimating outer ring KE. Vertical sensitivity (Figure S13) shows KE underestimations of 6.4–10.4% when truncating at −337 m. Most KE is concentrated in the upper 350 m, highlighting robustness to moderate vertical integration changes.

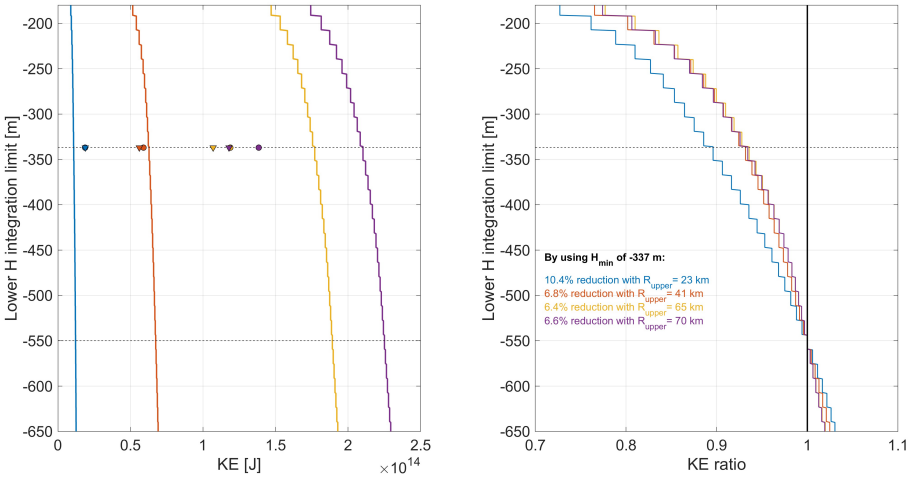


Figure S13: Same as Figure S11 but for integrated kinetic energy (KE) estimates.

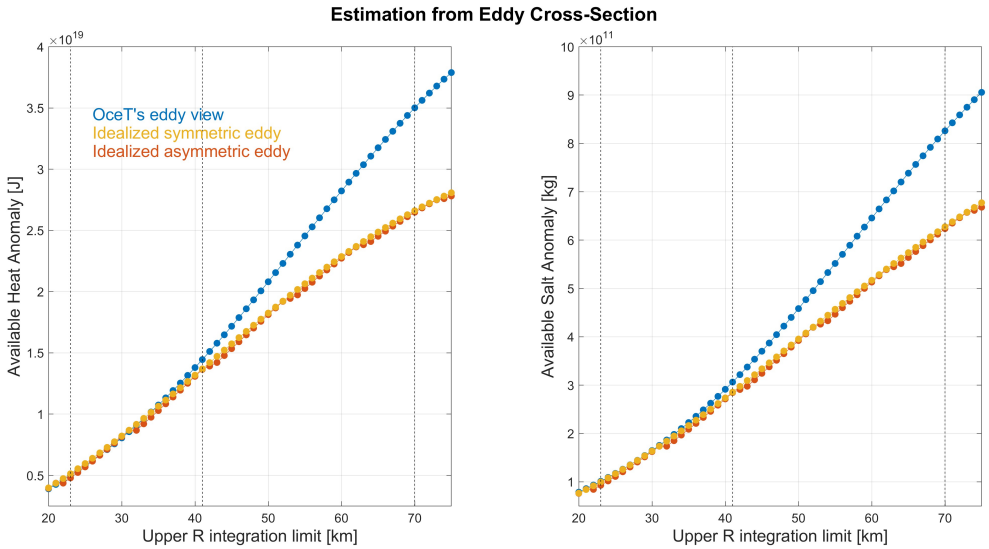


Figure S14: Same as Figure S10 but for integrated available heat anomalies (AHA, left) and salt anomalies (ASA, right).

Volume-integrated AHA and ASA exhibit similar radial sensitivity patterns to APE (Figure S14). For $R_{\text{upper}} \leq 30$km, differences between OceT and idealized sections are $< 3\%$, increasing to 25–26% at 70km. Vertical sensitivity analysis (Figure S15) indicates underestimations of 20–21% for AHA and up to 28.9% for ASA when using a −337m lower limit. AHA and ASA decline beyond ∼650–700m due to the presence of cooler, fresher diluted Antarctic Intermediate Water, which offsets the eddy anomalies.

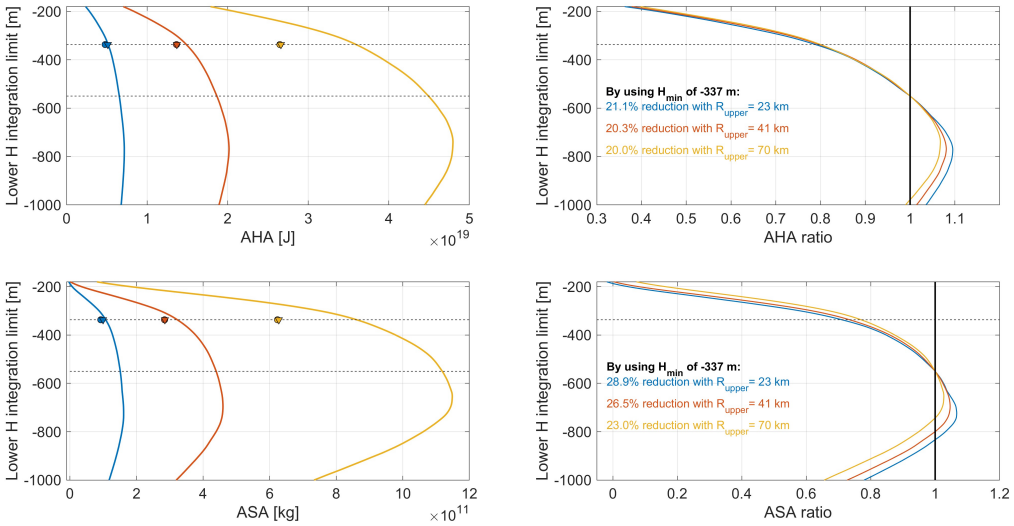


Figure S15: Same as Figure S11 but for Available Heat Anomaly (AHA; top panels) and Available Salt Anomaly (ASA; bottom panels). All estimates are based on the OceT dataset and use fixed upper radial limits of 23 km (blue), 41 km (red), and 70 km (yellow).

All metrics show consistent behavior: strong agreement across representations in the eddy core, increasing divergence in the outer ring. Differences stem from observational distortions, structural variability, and assumptions in idealized models. KE is less sensitive to vertical extent due to its confinement to shallower layers, while scalar anomalies like ASA are more susceptible to deep water variability. These findings support integrating within physically justified domains: the core ($R_c$) for compact energetics, or the full radius ($R_e$) for broader eddy influence.

# S5: Justification for core-limited integration using OceT

While the OceT section presents clear challenges in terms of synopticity, particularly due to its extended sampling duration and alignment with the eddy's translation, it offers the most complete vertical resolution among all available datasets. This attribute is essential for evaluating integrated energetic and scalar anomaly metrics (KE, APE, ASA, AHA), whose vertical sensitivity is non-negligible, as demonstrated in the Section S4.

To mitigate the radial distortion effects documented in Section S1, all integrations using OceT data are explicitly limited to the inner core domain ($|r| \leq R_c$), defined in Section S3 based on hydrographic consistency and low salinity variance. Within this domain, Doppler-induced deformation impact is constrained below 7%, and velocity profiles remain internally coherent across all quasi-synoptic transects, including those sampled along OceT.

This compromise leverages the superior vertical coverage of OceT while minimizing spatial bias by restricting the integration area to a dynamically consistent and geometrically stable core. The resulting energy and anomaly estimates are therefore interpreted as conservative lower-bound values for the full eddy, with minimal structural contamination. This strategy ensures comparability between observational and idealized estimates, as both use the same domain, and provides a defensible basis for interpreting energy budgets without overextending the spatial assumptions implicit in the OceT dataset.

# S6: Concluding remarks on methodological robustness

The results presented in this supplementary study provide the technical context and quantitative support for the methodological framework adopted in the main manuscript. Specifically, they address the potential structural distortion introduced by the non-synoptic nature of the OceT sampling configuration, quantify its impact through a Doppler-based analysis, and compare these outcomes with quasi-synoptic references obtained from the SeaSoar and orthogonal transects. The estimated deformation along the sampling axis—approximately 12.6% $\pm$ 6.2%—highlights the need to interpret OceT-derived gradients and integrated quantities with appropriate caution.

The construction of an azimuthally averaged, idealized eddy structure based on T3 and T4 transects offers a useful benchmark to assess the spatial consistency of hydrographic and kinematic patterns observed in OceT. Despite the expected limitations, key structural features—such as the well-mixed core ($|r| \leq R_c$)—demonstrate a high degree of reproducibility across independent datasets, supporting their validity for domain definitions in the energy and anomaly budgets.

Sensitivity analyses confirm that both radial and vertical integration limits influence the resulting energy and anomaly estimates. While inner-core metrics remain consistent across methods, values computed over extended radii or truncated depth ranges exhibit larger discrepancies. These outcomes emphasize the importance of spatial boundary definitions when comparing observational and idealized estimates.

Overall, this supplementary analysis enhances the robustness of the interpretations presented in the main article. By explicitly quantifying spatial distortion and exploring its effect on derived metrics, it provides a transparent basis for methodological choices and supports the general validity of the conclusions reached from the OceT dataset.

# S7: Supplementary Video – Life cycle of the Bentayga eddy

A video representation of the Bentayga eddy's life cycle is available at: https://doi.org/10.5446/69688 [Valencia and Aguiar-González, 2025].

This animation, based on the daily altimetric product META3.2exp and the sea level anomaly and geostrophic current fields derived from the CMEMS near-real-time altimetry product SEALEVEL_EUR_PHY_L4_NRT_008_060, illustrates the evolution of the eddy from its generation southwest of Gran Canaria Island in June 2022 to its state during the eIMPACT2 survey in November.

The video highlights the persistent proximity of other mesoscale vortices along the eddy's trajectory, providing qualitative support for the hypothesis of eddy–eddy interactions within the Canary Eddy Corridor.

# References


J.T. Allen, D.A. Smeed, A.J.G. Nurser, J.W. Zhang, and M. Rixen. Diagnosis of vertical velocities with the qg omega equation: an examination of the errors due to sampling strategy. *Deep Sea Research Part I: Oceanographic Research Papers*, 48(2):315–346, 2001. ISSN 0967-0637. doi: https://doi.org/10.1016/S0967-0637(00)00035-2. URL https://www.sciencedirect.com/science/article/pii/S0967063700000352.

Anthony Bosse, Ilker Fer, Henrik Søiland, and Thomas Rossby. Atlantic water transformation along its poleward pathway across the nordic seas. *Journal of Geophysical Research: Oceans*, 123(9):6428–6448, 2018. doi: https://doi.org/10.1029/2018JC014147. URL https://agupubs.onlinelibrary.wiley.com/doi/abs/10.1029/2018JC014147.

Anthony Bosse, Ilker Fer, Jonathan M. Lilly, and Henrik Søiland. Dynamical controls on the longevity of a non-linear vortex : The case of the lofoten basin eddy. *Scientific Reports*, 9, 12 2019. ISSN 20452322. doi: 10.1038/s41598-019-49599-8.

Liam Brannigan, David P. Marshall, Alberto C.Naveira Garabato, A. J.George Nurser, and Jan Kaiser. Submesoscale instabilities in mesoscale eddies. *Journal of Physical Oceanography*, 47:3061–3085, 12 2017. ISSN 15200485. doi: 10.1175/JPO-D-16-0178.1.

Leif N. Thomas, John R. Taylor, Raffaele Ferrari, and Terrence M. Joyce. Symmetric instability in the gulf stream. *Deep-Sea Research Part II: Topical Studies in Oceanography*, 91:96–110, 7 2013. ISSN 09670645. doi: 10.1016/j.dsr2.2013.02.025.

Luis P. Valencia and Borja Aguiar-González. Bentayga life-cycle as seen from satellite altimetry. Copernicus Publications, 2025.